ADVANCED MATERIALS TECHNOLOGIES
www.advmattechnol.de

Outdoor Stability of 518 cm^2 Active Area Screen-Printed Mesoscopic Carbon-Based Perovskite Solar Modules Over 12 Months

Sarah-Jane Potts, Rebecca Bolton, Carys Worsley, Tom Griffiths, Luke Ardolino, Kathryn Lacey, Ershad Parvazian, Eifion Jewell, and Trystan Watson*

Mesoscopic carbon-based perovskite solar cells (C-PSCs) composed of screen-printed TiO_2, ZrO_2, and carbon layers offer a pathway to stable, scalable, low-cost photovoltaics via commercially mature fabrication methods. While their potential lifespan has been demonstrated under standardized conditions, few studies examine the behavior of large-area modules exposed to real-world environments. Here, 12 months of outdoor weathering data are presented for 518 cm^2 active area $MAPbI_3$ modules with over 80% geometric fill factor, fabricated using low-cost mechanical scribing. Modules exhibited power conversion efficiencies (PCEs) up to 9.4% under 1 sun, with PCE increasing at lower light intensities. Following outdoor continuous intermittent power point tracking for over 12 months, an encapsulated module retained 68% of its initial PCE. Performance remained stable during cooler months, only falling when temperatures rose during summer months. Similar temperature-dependent trends are observed in repeated trials. Weathering trials identified key degradation pathways linked to fabrication—namely, non-uniform heating during perovskite annealing, encapsulation, and infiltration-related failures. Controlling heat exposure and conformity during module manufacture and operation is therefore critical to extending lifetime. These results highlight the importance of real-condition assessments in optimizing the scale-up of novel perovskite technologies, providing key insights into the steps required to achieve commercially viable lifetimes.

1. Introduction

Perovskite solar cells (PSCs) have advanced rapidly in recent years and are now capable of PCEs of 27% at 1 sun, making them comparable with traditional monocrystalline silicon devices.[1–3] However, lab-scale manufacture often relies on fabrication methods that are not easily scaled or expensive, such as spin coating. Device lifetime also presents a commercial viability barrier, as cells are sensitive to ambient moisture, oxygen, and temperature fluctuations.

Printed mesoscopic C-PSCs have the potential to meet these requirements, with champion cells recently exceeding 22% PCE.[4] These multi-layer devices consist of FTO glass with a compact TiO_2 layer, and sequentially screen-printed mesoporous films of TiO_2, ZrO_2, and carbon.[5–7] After the binder is removed, a lead halide precursor is infiltrated through the printed films, typically deposited via drop casting or inkjet printing, and heated to form the perovskite light-absorber.[8,9]

These devices are inherently scalable as screen-printing is a low capital expenditure (CAPEX), well established commercial process that is easily scaled. Consequently, industrial scale C-PSC modules fabricated using this method have already been presented in several works.[10–15] This has been heavily demonstrated at mini-module scale (10–200 cm^2), although there is a lack of studies exploring the sub-module range (200–800 cm^2) and above. Recent studies have demonstrated PCEs of 17.6% for an active area of 57.3 cm^2 and 12.1% for an active area of 70 cm^2 when measured unmasked.[16–18] When considering higher active areas, a study in 2018 scaled C-PSCs to 176 × 226 mm, with an active area of 198 cm^2 and PCE of 6% when measured unmasked.[13] Recently, the adoption of a relatively low-cost mechanical scribing method to separate adjacent cells increased the active area on this substrate size to 224 cm^2, pushing into the sub-module scale.[19] Coupled with print optimization and the adoption of non-toxic, better performing solvents, this resulted in PCEs of over 9% when measured unmasked.[20,21] To enable competitive power output to commercial modules, it is also essential to improve the geometric fill factor. This must ideally be achieved without significantly increasing

S.-J. Potts, R. Bolton, C. Worsley, T. Griffiths, L. Ardolino, K. Lacey, E. Parvazian, E. Jewell, T. Watson
SPECIFIC
Faculty of Science and Engineering
Swansea University
Bay Campus, Crymlyn Burrows, Swansea SA1 8EN, UK
E-mail: Sarah-Jane.Potts@Swansea.ac.uk

The ORCID identification number(s) for the author(s) of this article can be found under https://doi.org/10.1002/admt.202501313

DOI: 10.1002/admt.202501313

the manufacturing cost, as low CAPEX is one of the major advantages of this architecture.

Additionally, C-PSCs represent one of the most intrinsically stable perovskite device architectures. Through the addition of the additive 5-aminovaleric acid iodide (AVAI), C-PSC has demonstrated over 10 000 h stability in controlled standard conditions for a 50 cm^2 device.[22] This has been further supported by the development of encapsulation materials to prevent these devices from decomposing in the presence of heat and moisture.[23–25] These accelerated testing methods provide useful insight into device stability, but do not fully represent the reality of real-world environmental exposure.

In a relatively novel architecture whose degradation methods are not fully understood, external weathering is essential to identify and understand realistic failure. Early weathering studies have shown promise: 50 cm^2 active area AVAI/$MAPbI_3$ C-PSCs, glass-glass encapsulated with a silicon paste seal, have been externally tested for 12 months in France.[26] This trial was conducted from April to October, with modules remaining stable for the first three months when tested with maximum power point tracking (MPPT).

Epoxy resin encapsulated $MAPbI_3$ based C-PSCs have also been shown to remain stable for a week in the hot desert climate of Saudi Arabia, although there was a lack of external tests conducted beyond this stable period.[27] Additionally, more recent work has found that $CH_3NH_3PbI_{3-x}Cl_x$ based C-PSCs of 88 cm^2 active area, encapsulated with plastic panels and edge sealed with molten glue sticks, retained over 80% of the original PCE after 50 days of outdoor testing in Norway.[28]

These previous works provide insight into the behavior of smaller C-PSC modules in external conditions. However, it is unclear what performance and stability can be expected in larger scale modules tested over longer periods of time. Such modules may be more sensitive to early degradation, as defect prevalence increases with module area. external weathering of large-scale modules will therefore be essential in assessing the impact of low-cost manufacture on C-PSC modules and identifying potential long-term degradation or performance issues.

In this work, we present 300 mm × 300 mm C-PSC modules with an active area of 518 cm^2 and over 80% geometric fill factor (g-FF) (ratio between the active and the total printed area) produced with low-cost mechanical scribing. The optimized fill factor was achieved through optimizing the interconnect widths created with the mechanical scribing method. These devices were tested both internally in controlled conditions under simulated AM1.5G sunlight and externally in Port Talbot (Wales), with intermittent power point tracking to assess the impact of varying irradiance, temperature, and humidity over a year.

2. Results and Discussions

2.1. Module Structure

As outlined in **Figure 1**, the C-PSC module structure consists of three mesoporous screen-printed layers deposited onto FTO coated glass, which has been laser scribed to produce the P1 interconnect (Figure 1a,b). These P1 interconnects were created with a green laser to obtain the P1 scribe of ≈50 µm wide. This technique enables thorough removal of the FTO without damaging the glass, as previously reported.[13,29] Two further separations are required to create a series connected module, which were conducted with the affordable mechanical scribing technique.

P2 separates the sub-cells by removing all layers but the FTO, producing the required area for carbon-FTO contact. P3 then divides the carbon top contact to separate each cell's back electrode. This results in an inactive "dead area" comprising the sum of the interconnect widths and their separation distances, labelled Wd in Figure 1b. The P2 and P3 scribes could also be made with the same green laser that is used for the P1, as reported for other architectures.[19,30] However, perovskite is not infiltrated in the C-PSC at this stage; thus, no material can absorb visible light and protect the FTO layer. Additionally, the removal of the binder from the printed layers enables patterns to be easily created through the mesoporous layers without causing any damage to the FTO layer, making this low cost, simple technique a viable alternative for this architecture.

The amount of power a module of given substrate area can produce is intrinsically linked to the width of this dead area, which contributes significantly to the g-FF. Achieving smaller interconnect widths and separation distances is therefore required to maximize the power output of a module of given substrate area. These widths were optimized for this technique and architecture, based on previous studies.[19,31]

Mechanical scribing represents a more cost-effective alternative to producing narrow, steep sided interconnects using low-cost equipment. Fine sub-cell divides can be attained using laser scribing, but this requires more expensive, specialized laser equipment that increases manufacturing cost. To maintain low manufacturing costs, an intrinsic advantage of C-PSCs, this must be done using a low-CAPEX technique.

The P2 mechanical scribe was conducted following the heating of the m-TiO_2 and m-ZrO_2 layers and located ≈250 µm alongside the P1 interconnect. A P2 width of 500–550 µm was chosen as a compromise between the g-FF and providing sufficient area for electrical contact between the adjacent cells. This was required to enable the large graphite flakes within the mesoporous carbon layer to make contact, as well as account for the lower conductivity of the paste, when compared to traditional, more expensive alternatives such as gold, which require a narrower contact area. The m-carbon layer was then deposited and heated before the P3 scribe. The P3 scribe was positioned approximately 170 µm further from the P2 scribe and made ≈120 µm wide to provide an even and consistent separation across the cell lengths.

To ensure adequate cell separation, material removal, and measurement of the attained scribe widths, scribed modules were examined using white light interferometry to analyze surface topography and SEM/EDS for high-resolution analyses of the scribe edges. Images of the attained scribes in un-infiltrated stacks are presented in Figure 1c,d. As shown in Figure 1c, the mechanically scribed P2 is between 500 and 550 µm wide, with even removal of both the 0.8 µm m-TiO_2 and 0.94 µm thick ZrO_2 layers across the scribe width for the full length of the cells. The corresponding EDS analyses confirm that the underlying FTO layer

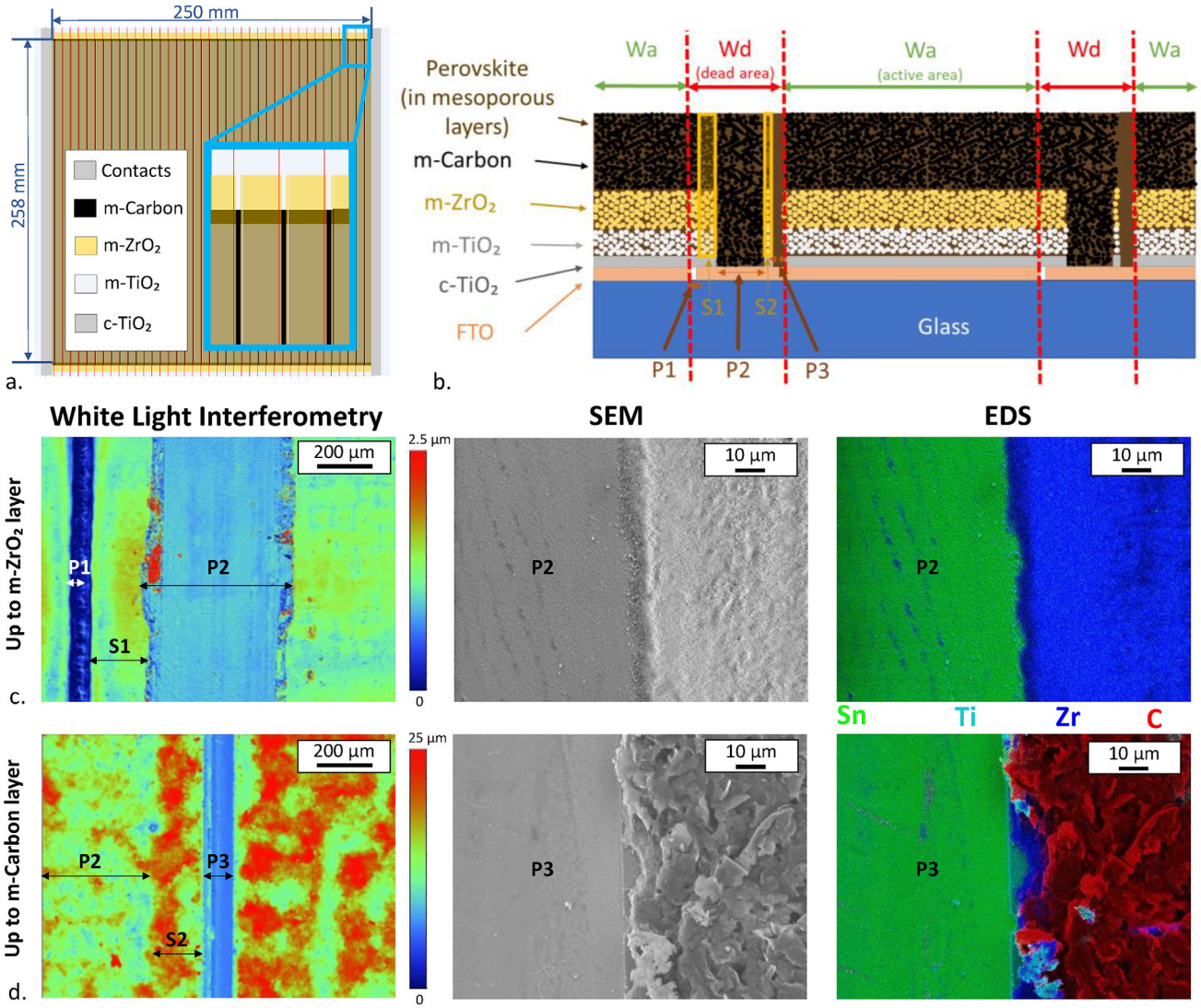

Figure 1. Module schematics, showing the different overlapping layers a) along with Cross-section schematics of adjacent cells in the module with nominal thickness of each layer, and b). Surface characterization of the interconnects on the mesoporous layers c) up to the m-ZrO_2 layer and d) up to the m-carbon layer. White light interferometry topography images of the surfaces of the prints at 5- times magnification are shown on the left. Scanning electron microscope (SEM) images showing the microstructures of the interconnect areas at 1000- times magnification are shown on the right, with corresponding EDS maps of the same sections.

is left undamaged, ensuring good electrical contact between m-carbon and FTO on subsequent deposition of the m-carbon layer. Similarly, the P3 scribe removed all mesoporous material without damaging the FTO, cleanly separating adjacent cells.

2.2. Module Performance and Weathering Data

Unmasked modules were assessed under 1 sun AM1.5G illumination in controlled, internal conditions before and after encapsulation. This was conducted to compare subsequent weathering data with a well-studied, industrial standard measuring process, as well as to identify whether the chosen encapsulation affected performance. For encapsulation, a PU sheet was first placed over the printed area before application of a butyl rubber edge sealant and glass cover.

As shown in **Figure 2**, prior to encapsulation, the average forward PCE of the modules was 7.9% ± 0.8, and the average reverse PCE was 7.2% ± 1.1, (Figure 2a). The champion module produced a forward PCE of 9.4% and showed relatively little hysteresis (Figure 2e). This module exhibited higher open-circuit voltage (V_{oc}) (34.6 V) and fill factor (FF) (46.7%) compared to the average values of 33.6 V ± 0.7 and 40.7% ± 3.4, which could be indicative of superior m-carbon-FTO contact. The reason for the spread of results is likely due to variations in printing conditions, scribe quality, and graphite orientation in the m-carbon layer. These results compare well with previous AVAI/$MAPbI_3$ C-PSC modules, where modules with a 198 cm^2 active area produced with the registration method achieved PCEs of up to 6.6%, and 224 cm^2

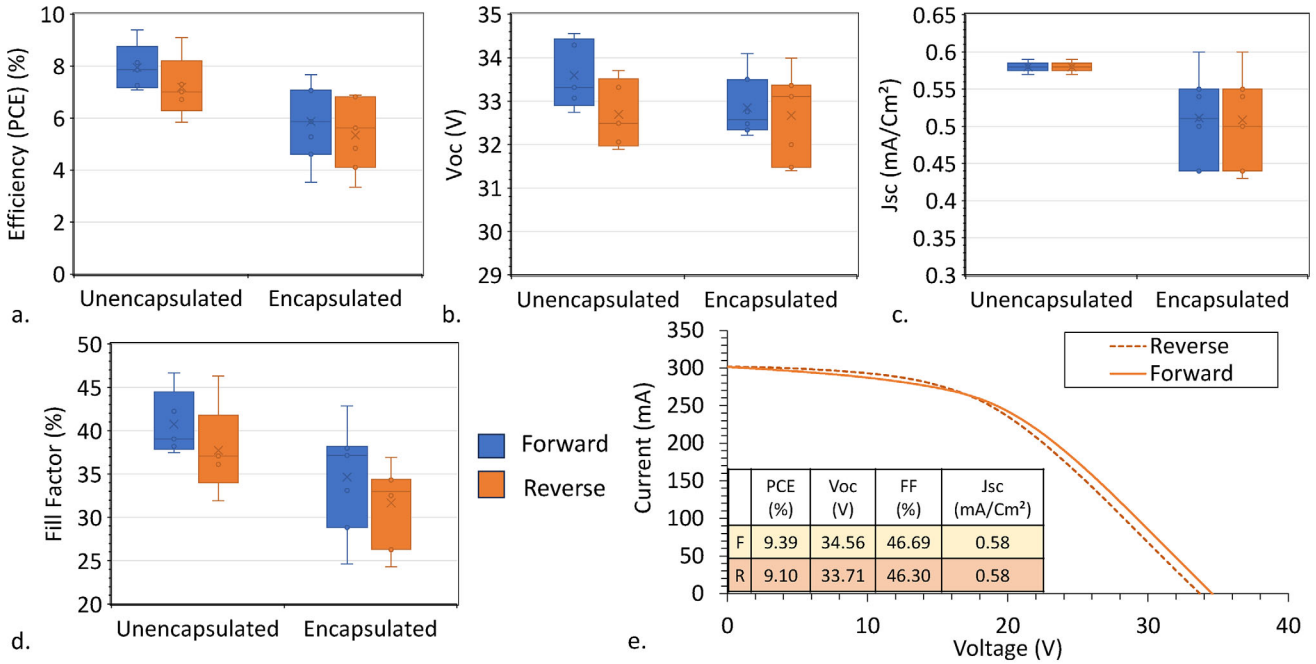

Figure 2. Box plot of IV PCE a), V_{oc} b), FF c), and J_{sc} values d) for the modules prior to and after encapsulation, under 1 sun (AM1.5), along with the IV curve of the champion device prior to encapsulation e).

modules produced with the mechanical scribing method achieved up to 9.9% PCE.[13,21]

After encapsulation, the average PCE dropped significantly to an average of 6.3% ± 1.5 and 5.8% ± 1.4 in forward and reverse, respectively, caused by a reduced FF and short-circuit current density (J_{sc}). It was posited that the high-temperature 120 °C encapsulation process may have induced some perovskite degradation, as it has been previously reported that heat-induced decomposition can occur even without moisture ingress.[32,33]

After indoor testing, modules were placed outdoors for external weathering (**Figure 3**). This was conducted at the Solar Heat Energy Demonstrator (SHED) in Port Talbot, UK, on an aluminum frame angled at 32° from horizontal, facing 160° South (pictured in Figure 3a). As a coastal location in South-West Wales, this area experiences high fluctuations in humidity and distinct seasonal weather variations. Ambient temperatures, module temperatures, humidity, and irradiance levels were continuously monitored. Module performance was continuously monitored using intermittent power point tracking during daylight hours, where IV sweeps were performed every 5 min with each module held at the maximum power point during the interval.

Collected external data was compared to solar simulator test results at multiple light intensities to ensure that the external testing setup produced comparable results. As shown in Figure 3b, there is good alignment between the external and solar simulator AM1.5 results for each of the key irradiance levels tested, validating the readings produced by this external testing method.

Initial weathering tests revealed some distinct causes of early degradation relating to issues in the manufacturing process. Where such defects were present, these would present as small grey or white perovskite free regions following curing of the perovskite. These would then act as a starting point for accelerated degradation after the thermal encapsulation process, subsequently developing into small, pale-yellow regions that expanded and became brighter yellow during the outdoor trials. Figure 3c and Figure 3di-diii show the modules after the first three months of outdoor testing. Figure 3c displays how the modules presented when they were evenly infiltrated and defect free, while Figure 3di-diii displays modules with signs of early degradation (pale-yellow regions), as a result of infiltration defects prior to encapsulation.

The module shown in Figure 3di initially displayed small grey and white perovskite free regions of around half a centimetre prior to encapsulation, which subsequently developed into the pale-yellow circles following external testing. The size and spacing of these circles corresponded with the location of the heating elements used during perovskite curing. The uneven heating and airflow during perovskite curing limited infiltration due to rapid crystallization in these areas, resulting in poor quality perovskite and some early heat induced MAI loss.[34–37] Previous studies found that this could be overcome by the application of a partial cover during perovskite annealing to reduce surface airflow and lower annealing temperatures to assist infiltration.[37,38] This method was applied to subsequently infiltrated modules, producing the consistent infiltration presented in Figure 3c. The module shown in Figure di also experienced one of the cells failing completely, as shown by the yellow strip. However, the module remained functional following this loss, suggesting that the modules are capable of bypassing failed strips. This suggests that the modules could be resilient to the output loss from damaged strips in practice and continue to function without these cells.

The other cases of significant degradation shown in Figure 3dii,diii, occurred due to uneven heat distribution

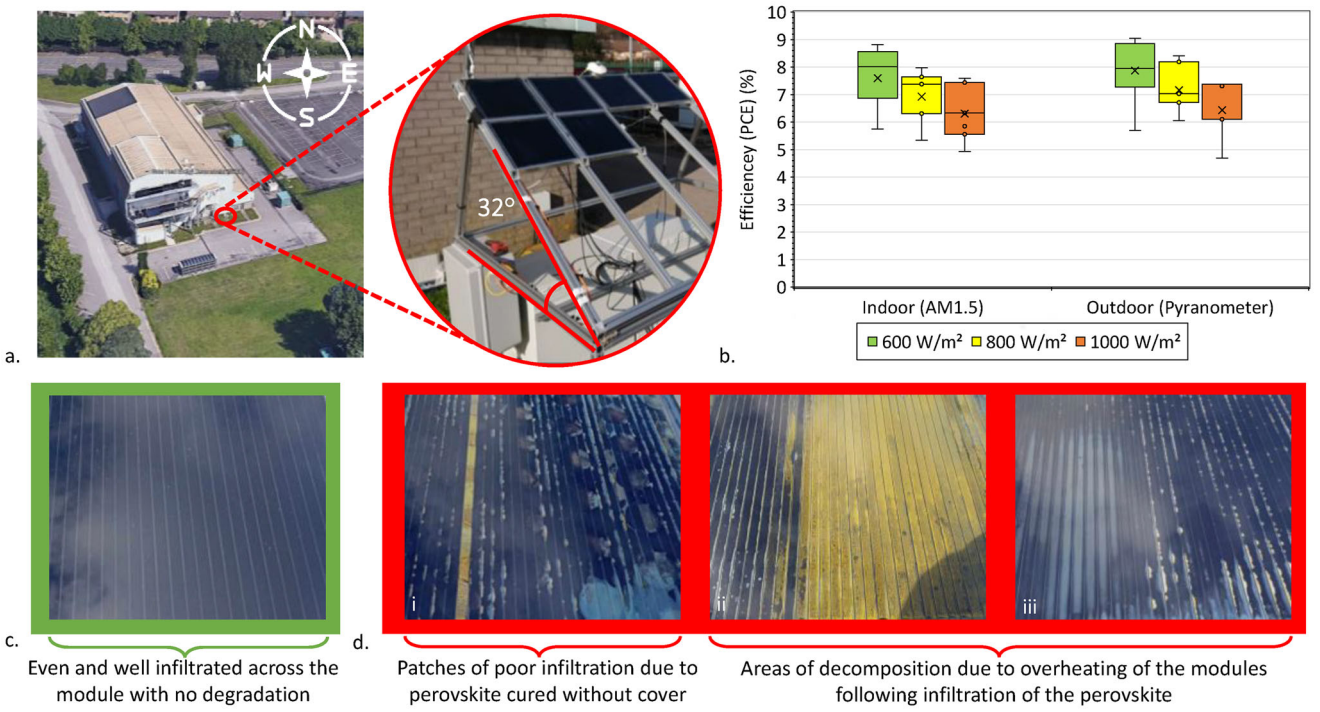

Figure 3. Outdoor Weathering station at the Solar Heat Energy Demonstrator (SHED) in Port Talbot, South Wales, showing the site's geographical orientation and a magnified image of the installed modules. a) Box plot of the I-V PCE of the encapsulated modules measured under at 1000, 800, and 600 W m^{-2} both indoors (AM1.5) and outdoors (pyranometer) b), alongside images of modules following 3 months of outdoor testing, including an evenly infiltrated module, with no degradation c) and examples of different observed degradation patterns (i to iii), due to uneven perovskite crystallization or thermal degradation d).

on the hot plate used for applying the PU sheet encapsulant. Interestingly, the modules with the greatest significant PCE reductions after the encapsulation process also experienced the most significant early degradation (Figure 2a). This confirms that the hot encapsulation method induced early degradation, suggesting that low temperature encapsulants may be more suitable for ensuring high module stability for this device structure. These visual analyses have demonstrated their benefit in identifying and addressing key failure mechanisms faced during the manufacture of these devices in previous studies.[34–37]

Poor perovskite infiltration, uneven temperature during curing, high airflow, and heating are all clearly detrimental to operational stability, producing significant defects under weathering. These findings align with other PSC studies, where inconsistent perovskite infiltration has been found to reduce device stability, as high densities of defects can cause increased recombination and lower lifespans.[34–37] This demonstrates the importance of optimizing the manufacturing techniques to ensure high-performing and long-lasting modules.

Where manufacturing related degradation issues were not visibly notable (as with Figure 3c), modules demonstrated impressive stability, with a T80 value (time to reach 80% of the initial PCE) of 3000 h (over 4 months). After a full year of testing, modules maintained 68% of the initial PCE. **Figure 4** displays the performance evolution of one module over 12 months of continuous monitoring. Data for both 0.6 sun (600 W m^{-2}) and 1 sun (1000 W m^{-2}) are presented. The data were continuously collected across all irradiance values, with recordings at these irradiance values (± 5 W m^{-2}) extracted for this comparison. The values on the graph display the change in average PCE, J_{sc}, $V_{oc,}$ and FF obtained at those irradiance values for each week of the year. Irradiance of 600 W m^{-2} was obtained throughout the assessed period, whereas 1000 W m^{-2} was only reached on some days between the first week of March and the third week of September on this first external trial. It is also worth noting that although the average values are presented here, it was found that the average PCE at a given irradiance level was typically higher in the morning than in the afternoon, as shown in Figure S1 (Supporting Information). This was consistent across the year, regardless of the seasons.

Over the first month, there was a ≈6% increase in PCE at 600 W m^{-2} due to a rapid increase in FF, while J_{sc} and V_{oc} remained relatively constant. Performance parameters then remained constant for another month before a gradual return to the initial PCE by the end of month three. This was then followed by a steeper decline from months three to eight, after which PCE stabilized at ≈68% of the initial value for the final five and a half months of testing. Performance losses were driven mostly by a gradual reduction in V_{oc}. FF also decreased somewhat but returned to its initial value for the remainder of the testing period. This data aligns with previous studies, where the PSC performance started declining during the warmer months due to reductions in V_{oc} and FF.[39,40]

Series resistance (R_s) remained relatively stable even during this degradation period, at 75–84 Ω for 600 W m^{-2} and 55–64 Ω at 1000 W m^{-2} (Figure S3, Table S1, Supporting Information). The

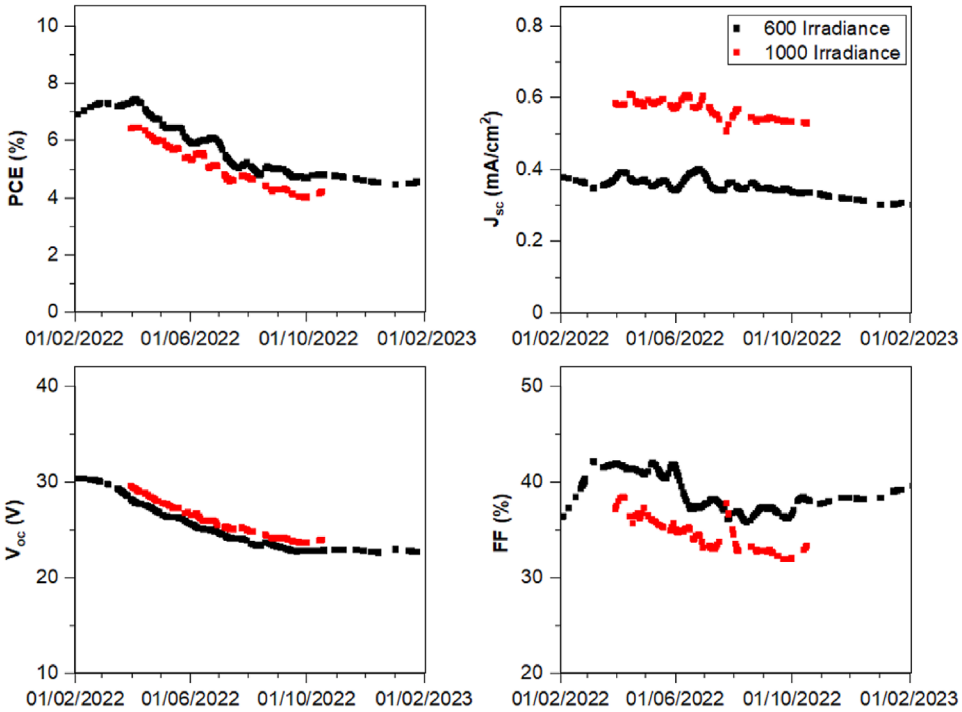

Figure 4. Solar parameters for the module from February 2022 to February 2023.

trend appears unrelated to temperature, with similar R_s at like irradiances between months with very different module temperatures. As R_s remained relatively stable over time despite performance losses and temperature fluctuation, it is most likely due to some physical aspect of the stack as opposed to the perovskite absorber. Limited carbon top contact conductivity or ineffective interconnect charge transport represent the most likely areas of high resistance. The latter could potentially be reduced with further scribe optimization, though this would likely require a more expensive laser setup. There may also be an intrinsic limit to the contact quality attainable between mesoporous carbon contacts and FTO.

Shunt resistance (R_{sh}) experienced a more significant change over the period of performance loss at both irradiances. Shunt resistance was lower at higher irradiance throughout, decreasing from 1351 Ω at 600 W m^{-2} to 465 Ω at 1000 W m^{-2}. This is typical of detrimental ion migration and increased trap filling and recombination at higher irradiance (Figure S3, Table S1, Supporting Information).[41] High recombination and trap density may be exacerbated in these modules as the $AVA_{0.03}PbI_3$ perovskite forms as small, polycrystalline grains. Modules made using highly controlled perovskite crystallization with alternative formulations may therefore prove more resilient toward shunts at high irradiance, although such methods have been proven difficult to scale and have very narrow processing windows.[42]

Although the decrease in R_{sh} over time would usually be ascribed to perovskite degradation, in the absence of any visual PbI_2 formation, partial perovskite delamination at charge extraction interfaces is more likely. This is a known issue in CPSCs, as the thermal expansion coefficient of perovskite is different to that of the mesoporous materials.[43]

The relationship between temperature and power output is presented in **Figure 5** for irradiances of 600 and 1000 W m^{-2} over the duration that higher irradiance was reached. Given that module weathering was performed in a coastal location, humidity fluctuations were experienced throughout the weathering period. Temperature, humidity, and irradiance values were collected instantaneously alongside IV readings throughout to provide directly corresponding values with the performance data.

Interestingly, module temperature remained ≈10 °C hotter than ambient temperature throughout the year, although this difference becomes less significant at lower irradiance levels, as shown in Figure S2 (Supporting Information). This is likely due to the dark color of the modules absorbing heat when subjected to direct sunlight. The reduction in power output began after the recorded module temperature exceeded 35 °C. However, it should be noted that the thermocouple was attached to the module's rear to prevent interference with their functionality. As the thermocouple was shaded behind the module and not subjected to direct sunlight, the true module temperature at which PCE reduction began was potentially slightly higher than 35 °C. This would align with the temperatures observed in previous studies on PSCs, which observed degradation starting at ≈40 °C.[39]

The recorded module temperature continued to increase up to 50 °C, with the rate of degradation slowing as the temperature reduced back down. The power output then stabilized when the recorded module temperature dropped back below 35 °C (Figure 5b). Degradation speed therefore, increases as temperatures rise. Reducing or controlling module temperature could therefore potentially prevent degradation and prolong lifespan.

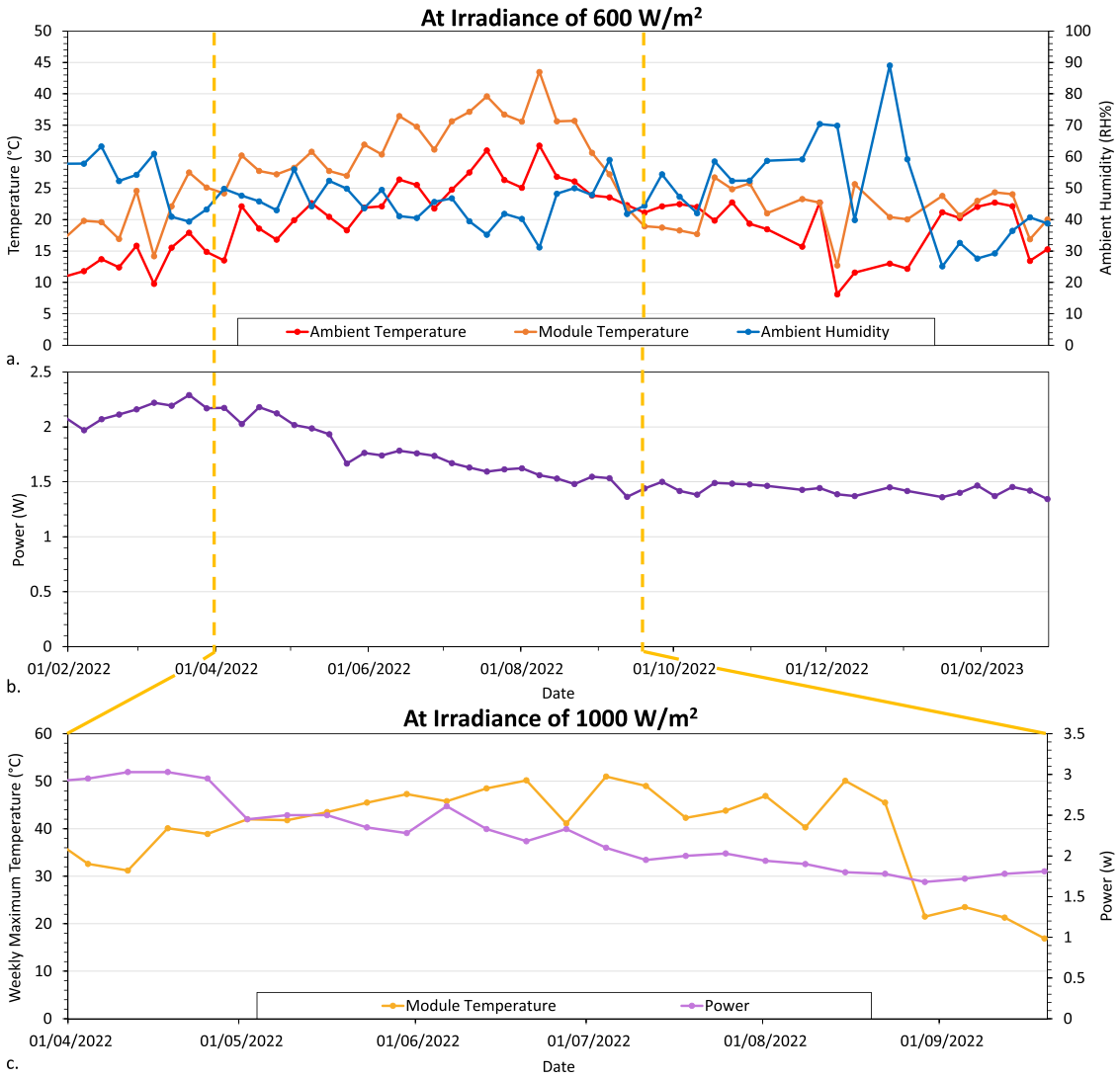

Figure 5. Changes in ambient temperature, module temperature, and ambient humidity a) with corresponding changes in power output b) recorded when the irradiance was equal to 600 W m^{-2} over a year, along with changes in the maximum module temperature recorded each week and the corresponding power output over the duration, recorded when the irradiance was equal to 1000 W m^{-2} c).

Although the thermal encapsulation process induced some PCE loss, the butyl rubber encapsulant proved effective in preventing moisture ingress. Despite the well-known detrimental impact of ambient humidity on performance,[14] no correlation between humidity levels and PCE was observed (Figure 5a). Thermal degradation was therefore the main driver in this case. Although the degradation was not reversible, in that performance did not recover at lower temperatures, it is encouraging that no further degradation was observed once temperatures dropped. Controlling module temperature should therefore significantly enhance lifetime.

Examining trends in photovoltaic performance parameters with irradiance can provide critical insight into performance loss mechanisms such as extraction and recombination.[41] **Figure 6** shows the relationship between performance parameters and irradiance at the beginning (February 2022), middle (August 2022), and end (February 2023) of the weathering process. Average panel temperatures were 16.45 ± 3.74 °C for February 2022, 34.54 ± 7.35 °C for August 2022, and 19.92 ± 5.84 °C for February 2023. As modules were not temperature controlled, higher irradiances were associated with increased temperatures, as indicated by the color mapping- most notable in Figure 6a. J_{sc} and V_{oc} plots were therefore filtered to prevent increased temperatures at higher irradiances inflating calculated parameters. Filtered and unfiltered datasets are presented in Figures S4 and S5 (Supporting Information). We note here that limited overlap in the attained panel temperatures between February and August necessitated the use of a higher temperature range filter- 26–30 °C for August and 16–19 °C for both Februarys.

The drop in PCE with time is relatively consistent across all irradiances, with lower irradiances producing higher PCEs throughout. PCE loss with irradiance occurs despite increasing J_{sc} and V_{oc}, offset by a significant loss in FF. As previously discussed, this is likely a consequence of high module series

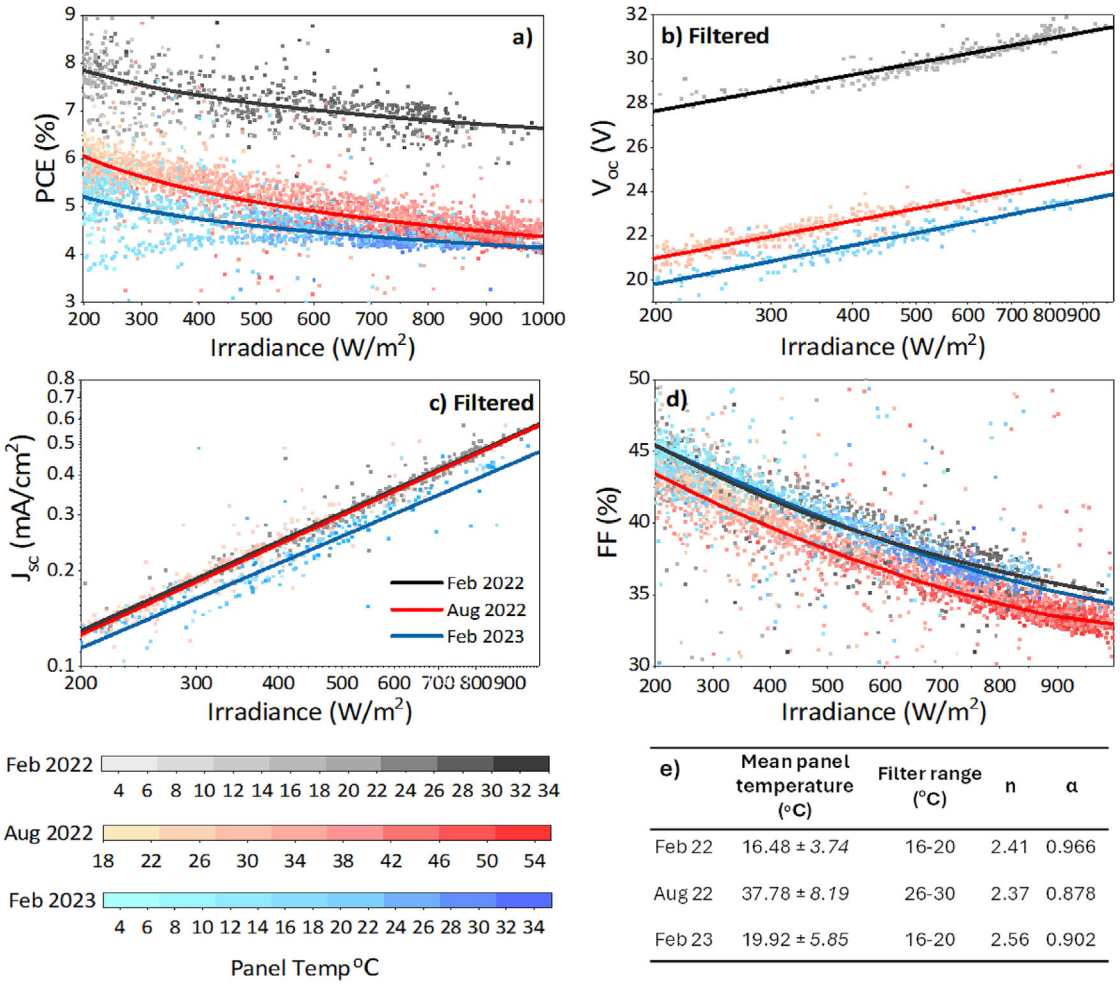

e)	Mean panel temperature (°C)	Filter range (°C)	n	α
Feb 22	16.48 ± *3.74*	16-20	2.41	0.966
Aug 22	37.78 ± *8.19*	26-30	2.37	0.878
Feb 23	19.92 ± *5.85*	16-20	2.56	0.902

Figure 6. Solar parameters a) PCE, b) V_{oc}, c) $J_{sc,}$ and d) FF) versus Irradiance at the start, after 6 months, and after 12 months of exposure with colormaps showing relevant temperature range for each period. J_{sc} and V_{oc} are filtered for n and α calculations presented in e).

resistance, which could potentially be overcome using more conductive carbon or further scribe optimization. As these particular modules perform better at lower light levels and temperatures, they may be more suited to indoor applications or locations that experience lower irradiances.

The overall trends with irradiance were relatively similar for all three months, the greater change being in the absolute values of each performance parameter. This is most notable in the V_{oc} data, where the most significant drops over time are observed. This is particularly significant when comparing values for February 2022 and 2023 in Figure 6b, where like data filtering reduces the influence of temperature on the gradient. The ideality factor "n", obtained from the gradient of this plot, increased from 2.41 in February 2022 to 2.56 in February 2023. The apparent decrease during August 2023 is due to higher panel temperatures and is therefore not comparable. Values of "n" greater than 2 indicate significant trap assisted recombination, interfacial issues, or shunts. Increasing "n" over time suggests that these issues are worsening, though not from where they originate. Realistically, this could be caused by slow degradation or partial interface delamination anywhere in the stack.

Similarly, the slope (α) of the relationship between short-circuit current (Jsc) and irradiance was calculated as 0.966 for the fresh module in February 2022 and decreased to 0.902 by February 2023. August 2022 produced a lower value of 0.878, but this was likely influenced by higher panel temperatures. An $\alpha<1$ has been shown to indicate recombination or extraction losses.[41] Recombination or extraction inefficiencies are therefore increasing over time, though it must be stressed that the precise location or driver of these losses cannot be determined from these data.

Modules clearly demonstrated a significant performance loss with temperature, driven by gradual voltage loss during periods where panel temperatures exceeded 35 °C. To assess whether these trends would be reproduced in future years, other modules from this batch were tested again in 2024 (24 months after manufacture) (**Figure 7**). In the intervening time, the modules were stored in a dark, clean environment and only encapsulated prior to being tested outdoors.

Normalized PCEs at 600 W m^{-2} from 2024 are presented alongside those from 2022 in Figure 7a. The results were normalized against their initial value on being installed externally to

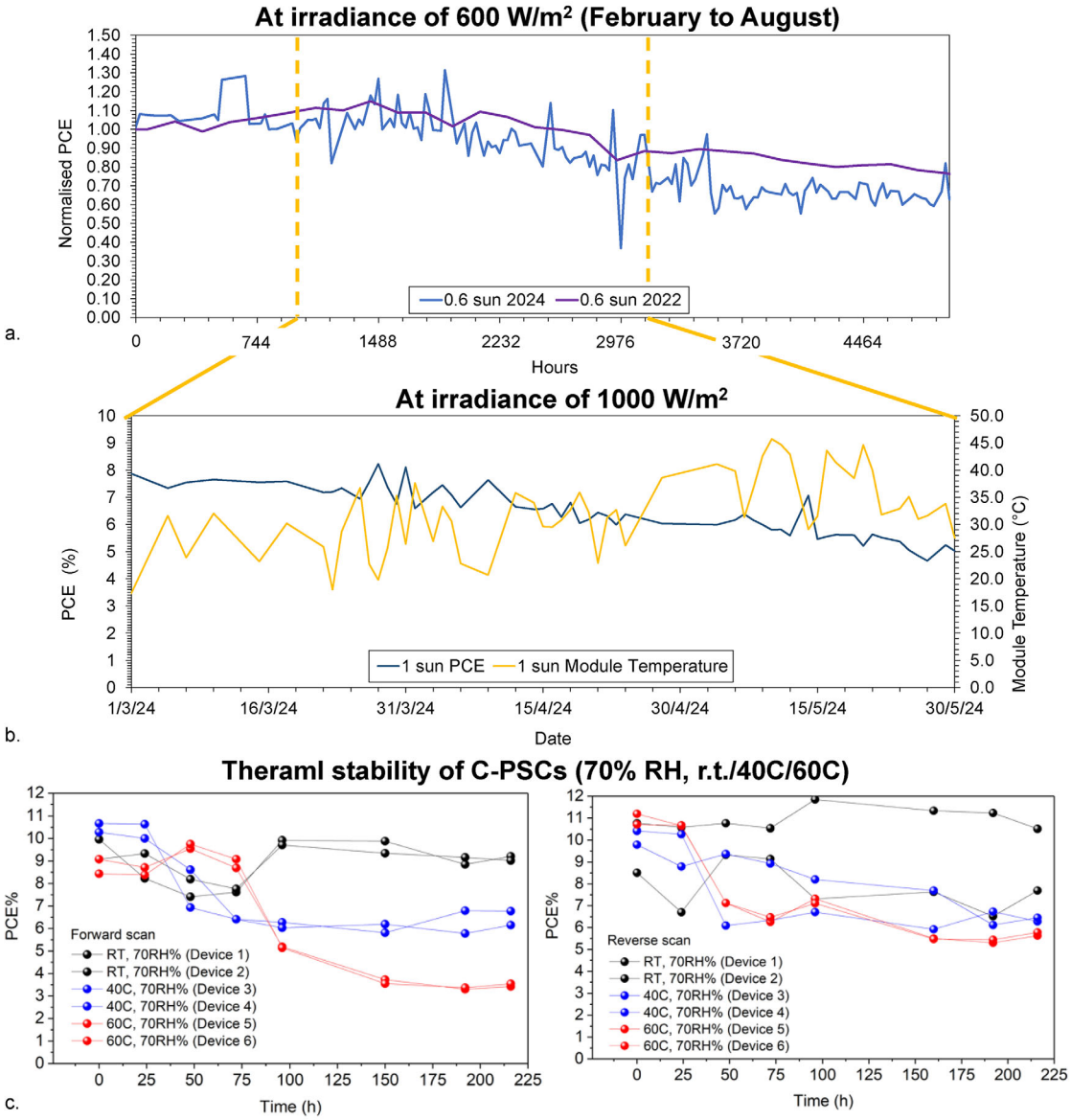

Figure 7. Comparison in the normalized PCE recorded when the irradiance was equal to 600 W m^{-2} for modules tested in 2022 and with others tested in 2024 over the same months a), with corresponding changes in module temperatures against the measured PCE for 2024 recorded when the irradiance was equal to °0 W m^{-2} b) and the normalized PCE of cells held under controlled conditions at room temperature, 40 and 60 °C then tested indoors (AM1.5) forward c) and reverse d) directions at regular intervals.

provide a direct comparison of PCE loss over the testing duration. Figure 7b, which compares the module PCE at 1000 W m^{-2} with the corresponding module temperature. Once again, a notable decline in performance is observed during periods where daily peak module temperatures (at 1000 W m^{-2}) range between 35 to 45 °C. As with the initial trials, the PCE then stabilized when the module temperature readings dropped back below these values, aligning with the trends shown in Figure 5b. There was also no correlation between humidity levels and PCE (Figure S2, Supporting Information), aligning with the trends seen in 2022.

The impact of elevated temperature on the device PCE loss was also assessed under controlled conditions on encapsulated 1 cm^2 cells of the same architecture, to isolate the impact of temperature from the other external factors, such as humidity (Figure 7c,d). The PCE of six cells was assessed under 1 sun (1000 W m^{-2}) AM1.5G illumination in controlled, internal conditions and normalized for direct comparison. The devices were held at room temperature, 40 and 60 °C for up to 225 h, as shown in Figure 7c,d. The devices were held under these conditions in darkness and taken out daily for testing to isolate the impact of temperature on their performance.

The cells held at room temperature initially fluctuated in PCE, but then remained relatively stable after 100 h, with at least 90% of the original PCE retained. The devices held at 40 °C demonstrated a more significant loss of performance, with ≈60% of the original PCE retained after 225 h. As 40 °C was the average

recorded module temperature reached during the hotter months of outdoor testing, this provides a useful comparison, with a similar PCE loss demonstrated on the cells to the externally tested modules. However, other countries experience notably higher temperatures than the UK, so the cells were also tested at 60 °C. In this circumstance, only ≈35–55% of the original PCE was retained. This outcome further demonstrates the impact of temperature on module performance and the need to tailor future developments of PSC architectures to ensure prolonged thermal stability.

Overall, the weathering data presented in this work represent the first full-year analysis conducted on a large scale $MAPbI_3$ based C-PSC manufactured with affordable and commercially mature methods. This provides valuable insight into the impact of a full season of true outdoor conditions. After a full year of weathering, the module retained 68% of its initial PCE, having remained stable at this value for five and a half months from mid-September 2022 to the final Week of February in 2023. This included remaining stable during very low temperatures across the winter months. This highlights the high potential of this architecture for future commercial applications, as well as the challenges required to achieve commercially viable lifetimes. When tests were repeated on other modules from the batch two years later in 2024, similar trends were shown, with the modules once again retaining ≈68% of their initial PCE, after the hotter months had passed. These results correspond with other studies conducted on perovskite solar cells of different architectures, which also saw a drop in performance at similar temperatures when tested both indoors and outdoors.[26,39,40,43]

Interestingly, while the encapsulated modules were not impacted by ambient humidity, thermal degradation was found to be particularly detrimental to lifetime, driving irreversible PCE losses during warmer months. Indeed, high temperature exposure prior to, during, and after encapsulation has all been shown to negatively impact lifetime. Infiltration defects caused by uneven temperature and airflow during perovskite annealing were also found to significantly reduce module lifetime. In this case, degradation observed in the modules is most likely not solely due to degradation of the perovskite, as the modules that underwent long term testing demonstrated minimal color change. Although the modules that experienced manufacturing related defects demonstrated yellowing, this was not seen on the modules that survived the year, with them going grey rather than yellow in most cases. This could be due to the thermal expansion coefficient mismatch between the perovskite and the m-TiO_2 electron transport layer, causing significant interface strain between the perovskite and the m-TiO_2, as reported in the literature.[43] This strain was found to cause delamination with temperature exposure, which manifests as irreversible performance loss in the absence of color change, as observed here. The impact of this is likely greater as module size increases. Future work could utilize the International Summit on Organic Photovoltaic Stability (ISOS) protocols to further assess the thermal stability of large-scale modules to tailor future external trials, such as ISOS-D-2 tests, which have previously been applied to smaller scale devices.[44,45]

It is therefore critical to explore methods that minimize heat exposure during module encapsulation and operation, as well as taking steps during manufacture to limit potentially detrimental infiltration defects.

3. Conclusion

Series connected, 518 cm^2 active area triple mesoscopic C-PSC modules with a g-FF of over 80% were successfully manufactured using mechanical scribing, an affordable and commercially mature manufacturing method. The unmasked champion module reached 9.4% PCE when tested indoors at AM 1.5 under 1 sun.

Encapsulated modules were then placed for external weathering, in Wales, UK. This revealed key issues in the manufacturing process that drive degradation, with uneven heating and airflow during perovskite annealing, infiltration defects, and heated encapsulation steps all causing early performance losses.

Optimized modules were able to sustain 68% of the original post encapsulation PCE after 12 months of outdoor testing, with similar trends shown on repeat trials under the same conditions. Performance losses were driven by heat exposure in the summer months: Modules remained at the original PCE for three months, only experiencing degradation once daily maximum recorded module temperatures exceeded 35 °C. Controlling module temperature during fabrication and operation is therefore critical to preventing performance losses. Notably, once module temperatures were reduced, no further performance losses occurred for the remaining 5.5 months of weathering. Indeed, in the absence of high temperatures, modules were exceptionally stable over multiple months of continual exposure and IV cycling. This result indicates that this perovskite architecture is a good candidate for future commercial ventures in low-cost perovskite solar technology.

4. Experimental Section

Manufacturing of Photovoltaic Modules: To fabricate the 518 cm^2 active area modules, FTO substrates (FTO glass TEC-7 2.2 mm, XOP Glass) were patterned with a Rofin Nb: YVO_4 laser (532 nm) at a speed of 150 mm s^{-1} to create the P1 scribe interconnect. These were then cleaned with approximately 2% Hellmanex solution in deionized water, washed with deionized water, and rinsed with acetone and IPA, then dried with N_2. To deposit the compact TiO_2 layer, the substrates were then heated to 300 °C on a hot plate, and a solution of titanium diisopropoxide bis (acetylacetonate) (TAA, 75% in IPA, Sigma–Aldrich) with anhydrous 2-propanol (IPA, 99.5%, Sigma–Aldrich) was deposited by spray pyrolysis.

All layers of the triple mesoporous stack were deposited via screen-printing on an ATMA 1400 semi-automatic screen-printing press. Each printed device was dried in a Thieme hot dryer at 100 °C for a residence time of 20 min, then cured in a HENGLI Belt Furnace. The TiO_2 layers were diluted 1:0.75 by weight with terpineol were printed with a polyester mesh at 45° with 130 threads per cm, 34 µm thread diameter, and 9-µm emulsion over mesh (EOM). A 70–75 Shore A hardness blade squeegee of 500 mm length was used, along with a snap distance (distance between screen and substrate) of 5 mm and squeegee travel speed of 700 mm s^{-1}. These were then sintered at 550 °C for 30 min after a slow ramp. The ZrO_2 ink (Zr-Nanoxide ZT/SP, Solaronix) was printed with the same mesh, squeegee, and print speed as the TiO_2 ink, which was then sintered at 400 °C for 30 min after a slow ramp. The carbon ink (GEM C2150317D3 carbon paste (Gwent Electronics Materials (GEM)), diluted with 5 wt.% 1-Methoxy-2-propanol (Sigma)) was printed with a polyester mesh at 45° with 61 threads per cm, 64 µm thread diameter, and 12 µm emulsion over mesh (EOM). A 65–70 Shore A hardness blade squeegee at 30° to the

Table 1. Average widths of the scribed interconnects and gaps between them within the dead area between the cells (standard deviation given in brackets).

Features		Average width [µm]
Scribed	P1	72 (±2)
Interconnects	P2	526 (±25)
	P3	119 (±7)
gap	S1	249 (±67)
	S2	169 (±45)

mesh was used, with the same print speed and snap distance as before. As with the ZrO_2 inks, these were then sintered at 400 °C for 30 min after a slow ramp. The measured mesoporous layer thicknesses were 0.8, 2, and 10 µm for TiO_2, ZrO_2, and carbon, respectively.

The P2 and P3 scribes to create the interconnects in the other layers were conducted on a Workbee CNC instrument with a steel blade under 0.54 N mm^{-1} pressure, to mechanically create the patterns. The average width of the interconnects and the gaps between them are summarized in **Table 1**, and the average width and surface roughness of the mesoporous layers in **Table 2**.

The average surface roughness of the printed layers was relatively low, compared with analyses of the mesoporous layers in previous works.[21,46] This can be observed in the white light interferometry images (Figure 1c,d) and is summarized in Table 2. This was particularly important in larger scale prints where regions of poor infiltration can have a significant impact on performance. The high uniformity of these large prints was achieved through careful optimization of press print pressures, speeds, and snap-off distances, and manipulation of ink rheological profiles to minimize print defects, as presented in previous works.[21,47,48] This should ensure homogeneous perovskite precursor infiltration and thus improve module reproducibility, PCE, $V_{oc,}$ and FF.

Once scribed, the modules were then infiltrated with perovskite solution. All layers were cooled to room temperature in ambient conditions (30–50% RH, 18–21 °C), then the perovskite precursor (containing PbI2 (99%, TCI), MAI (CH_3NH_3I, anhydrous, Greatcell Solar), 5- ammonium valeric acid iodide (5-AVAI, Greatcell Solar), g-valerolactone (GVL, Sigma–Aldrich) and anhydrous MeOH (Sigma–Aldrich)) was deposited via a LOCTITE 400D deposition robot at a speed of 12 m s^{-1} with a 12-gauge syringe tip at 1 bar of pressure. Devices were left for 20 min in ambient conditions to ensure adequate infiltration before annealing in a Thieme conveyor dryer at 45 °C for 1.5 h. Contacts were applied manually via ultrasonic soldering at 180 °C, and robotic wires were subsequently soldered to the contacts. The completed devices were then heated on a hot plate to 120 °C, and a PU sheet was applied to cover the active area and contacts. The devices were cooled before the edge seal butyl rubber (Quanex, SET LP03: 2 mm thick) was applied, sealing the modules to a sheet of backing glass.

The completed modules consisted of 39 cells, each 5.25 mm wide and 258 mm long, spaced ≈6.5 mm apart when accounting for the total scribed width (as shown in Figure 1a). A border of ≈1 cm of excess substrate was provided to allow for edge seal encapsulation. This resulted in an active area of ≈518 cm^2, with a g-FF of over 80% g-FF across the designated area of the module.

Manufacturing of Photovoltaic Cells: To fabricate the 1 cm^2 cells, FTO substrates (FTO glass TEC-7 2.2 mm, XOP Glass) were patterned with a Rofin Nb:YVO4 laser (532 nm) at a speed of 150 mm s^{-1}. These were then cleaned with approximately 2% Hellmanex solution in deionized water, washed with deionized water, and rinsed with acetone and IPA, then dried with N2. To deposit the compact TiO_2 layer, the substrates were then heated to 300 °C on a hot plate, and a solution of titanium diisopropoxide bis (acetylacetonate) (TAA, 75% in IPA, Sigma–Aldrich) with anhydrous 2-propanol (IPA, 99.5%, Sigma–Aldrich) was deposited by spray pyrolysis. All layers of the triple mesoporous stack were deposited via screen-printing on an ATMA AT-25PA flatbed screen printer. Each printed sample was dried in a Thieme hot dryer at 100 °C for a residence time of 20 min, then cured in a HENGLI Belt Furnace.

The mesoporous layers were printed with the same pastes and dilutions as specified in manufacturing the modules (above). The TiO_2 layers were printed with a polyester mesh at 45° with 130 threads per cm, 34 µm thread diameter, and 9-µm emulsion over mesh (EOM). A 70–75 Shore A hardness double bevel blade squeegee of 130 mm length was used, along with a snap distance (distance between screen and substrate) of 3.3 mm and squeegee travel speed of 210 mm s^{-1}. These were then sintered at 550 °C for 30 min after a slow ramp. The ZrO_2 ink was printed with the same mesh, squeegee, and print speed as the TiO_2 ink, but with a 4.3 mm snap distance. These were then sintered at 400 °C for 30 min after a slow ramp. The carbon ink was printed with a polyester mesh at 45° with 61 threads per cm, 64 µm thread diameter, and 12 µm emulsion over mesh (EOM). A 65–70 Shore A hardness blade squeegee at 30° to the mesh was used, along with a snap distance (distance between screen and substrate) of 4.3 mm, with the same print speed as before. As with the ZrO_2 inks, these were then sintered at 400 °C for 30 min after a slow ramp. Each of the mesoporous layers was cured individually to ensure the binder was thoroughly removed from the mesoporous layers. The curing steps were conducted separately for each layer to ensure maximum removal of the binders and to minimize the creation of defects in the printed layer topology, such as pinholes, agglomerations, and cracks in the print microstructure, as found in literature.[21]

All layers were cooled to room temperature in ambient conditions (30–50% RH, 18–21 °C), before drop casting of 20 ml room temperature perovskite precursor (same formulation as specified for the modules) onto the stack. Devices were left for 20 min in ambient conditions after drop casting the precursor to ensure adequate infiltration, before annealing on a hot plate for 1.5 h at 45 °C. Contacts were applied with an ultrasonic solder at 180 °C.

Characterization of Print Topography: White light interferometry (NT9300, Veeco Instruments, Inc., Plainview, NY, USA) was used to measure a full 3D surface profile of the mesoporous screen-printed layers. 5× magnification was used for printed film thickness and roughness analyses, giving a measurement area of 1.2 mm by 0.93 mm (at a resolution of 736 × 480 pixels with sampling at 1.67 µm intervals). The print film thickness was evaluated by measuring over the edge of the solid print, calculated as the average thickness of the substrate subtracted from the average thickness of the ink.

Scanning Electron Microscopy: The microstructure of the prints was assessed using a JEOL JSL 7800F FEG scanning electron microscope (SEM). Top-down images of the mesoporous layers were conducted on samples that were sputter coated in 5 nm of Pt to enhance conductivity, in secondary electron scanning mode with an electron energy of 10 kV, a working distance of 10 mm, at a magnification of 1000×. The chemical analyses were performed using an Oxford Instruments Ultim energy-dispersive X-ray spectroscopy (EDS) detector with an AZTEC software (Ver 5.0) analysis package (Oxford Instruments Plc, Abingdon, UK), at a 10 mm working distance.

Solar Simulator Testing of Photovoltaic Modules: Modules were left unmasked and placed under a fan for testing. A Keithley 2440-C source meter and class AAA solar simulator (G2V Sunbrick solar simulator, capable of testing up to 625 cm^2) at 1 sun was used for J–V measurements (calibrated against a KG5 filtered silicon reference cell, Newport Oriel 91150-KG5). Devices were scanned at a rate of 0.126 V s^{-1} from V_{oc} to J_{sc} and vice versa after a light soaking period of 180 s. For stabilized current measurements, devices were held at the maximum power point (as determined by the preceding IV scan) for a period of 200 s to account for slow response times. This was conducted on 5 separate modules.

Solar Simulator Testing of Photovoltaic Cells: The cells were masked to 0.16 cm^2 and tested with a Keithley 2400-C source meter and class AAA solar simulator (G2V Sunbrick solar simulator) at 1 sun was used for J–V measurements (calibrated against a silicon reference cell, Newport Oriel 91 150 V). Devices were scanned at a rate of 100 mV $s^{\mp 1}$ from −0.2–1.1 V and vice-versa after a light soaking period of 180 s. To assess the impact of elevated temperatures, cells were held under controlled conditions at

Table 2. Average printed film heights and roughness of the mesoporous printed layers (standard deviation given in brackets).

Layer	Average print height [µm]	Average surface roughness [Sa] [µm]	Maximum surface roughness [Sz] [µm]
TiO_2	0.8 (±0.15)	0.017 (±0.002)	0.44 (±0.02)
ZrO_2	0.94 (±0.04)	0.28 (±0.008)	5.9 (±0.2)
Carbon	8.3 (±0.2)	1.32 (±0.005)	23.6 (±6)

room temperature, 40 and 60 °C. The devices at room temperature were stored in an airtight box in darkness between tests, while devices tested at elevated temperatures were held in humidity ovens at 40 and 60 °C at 70RH% in darkness between tests. The devices were taken out daily for testing.

Outdoor Weathering Station: The encapsulated modules were mounted onto an aluminum framework angled at 32° from horizontal, facing 160° South on 21st January 2022 for the first batch of tests, and then on 21st January 2024 for the second batch of tests, at the Solar Heat Energy Demonstrator (SHED) in Port Talbot, UK. Each module was connected to a TENMA 72–13210 for DC loading and an ICP DAS PET7017-10 thermocouple module for panel temperature tracking. The whole station was equipped with an in-plane Kipp & Zonen SMP-3 pyranometer for irradiance recording and DL-10 sensor for ambient temperature/humidity monitoring connected to an ICP DAS TGW-715 Modbus RTU-TCP Gateway.

During daylight hours (06:00-19:00 UTC), each module was subject to "intermittent power point tracking" which involves an IV sweep between V_{oc} and I_{sc} every 5 min. Modules were then held at the maximum power point until the next sweep. Irradiance, panel temperature, ambient temperature, and ambient humidity were continuously monitored.

Supporting Information

Supporting Information is available from the Wiley Online Library or from the author.

Acknowledgements

The authors acknowledge funding from the Prosperity Partnership through EPSRC (EP/X025217/1) and Royal Society International Collaboration award (ICA\R1\191321). Additional support was received via the EPSRC Programme Grant ATIP (Application Targeted and Integrated Photovoltaics) (EP/T028513/1). Microscopy facilities were provided by the Swansea University AIM Facility; funded in part by the EPSRC (EP/M028267/1). The authors also thank the Welsh Centre for Printing and Coating for access to the white light interferometer. The manuscript was written through the contributions of all authors. All authors have given approval to the final version of the manuscript.

Conflict of Interest

The authors declare no conflict of interest.

Data Availability Statement

The data that support the findings of this study are available from the corresponding author upon reasonable request.

Keywords

mechanical scribing, outdoor testing, perovskite solar modules

Received: June 20, 2025
Revised: August 25, 2025
Published online:

[1] F. Ma, Y. Zhao, Z. Qu, J. You, *Accounts Mater Res* **2023**, *4*, 716.
[2] NREL. Interactive Best Research-Cell Efficiency Chart | Photovoltaic Research | NREL, **2025**, https://www.nrel.gov/pv/interactive-cell-efficiency.
[3] T. Wu, P. Wang, L. Zheng, Y. Zhao, Y. Hua, *Adv. Energy Mater.* **2024**, *14*, 1.
[4] J. Liu, X. Chen, K. Chen, W. Tian, Y. Sheng, B. She, Y. Jiang, D. Zhang, Y. Liu, J. Qi, K. Chen, Y. Ma, Z. Qiu, C. Wang, Y. Yin, S. Zhao, J. Leng, S. Jin, W. Zhao, Y. Qin, Y. Su, X. Li, X. Li, Y. Zhou, Y. Zhou, F. Ling, A. Mei, H. Han, *Science* **2024**, *383*, 1198.
[5] S. M. P. Meroni, C. Worsley, D. Raptis, T. M. Watson, *Energies* **2021**, *14*, 386.
[6] J. Jestine, R. E. Johnston, C. P. Pearce, P. Davies, T. Watson, S. Meroni, C. Worsley, R. Dimitrios, T. Dunlop, R. Mitchell, T. Volkenandt, B. Tordoff, S. Kelly, R. White, M. N. Rad, *Microsc. Microanal.* **2022**, *28*, 204.
[7] D. Pourjafari, N. G. García-Peña, W. Y. Padrón-Hernández, D. Peralta-Domínguez, A. M. Castro-Chong, M. Nabil, R. C. Avilés-Betanzos, G. Oskam, *Materials (Basel)* **2023**, *16*, 3917.
[8] J. Baker, K. Hooper, S. Meroni, A. Pockett, J. McGettrick, Z. Wei, R. Escalante, G. Oskam, M. Carnie, T. Watson, *J. Mater. Chem. A* **2017**, *5*, 18643..
[9] A. J. Huckaba, Y. Lee, R. Xia, S. Paek, V. C. Bassetto, E. Oveisi, A. Lesch, S. Kinge, P. J. Dyson, H. Girault, M. K. Nazeeruddin, *Energy Technol.* **2019**, *7*, 317.
[10] J. Kang, H. Kim, K. S. Kim, S.-K. Lee, S. Bae, J.-H. Ahn, Y.-J. Kim, J.-B. Choi, B. H. Hong, *Nano Lett.* **2011**, *11*, 5154.
[11] A. Morrin, A. J. Killard, M. R. Smyth, *Anal. Lett.* **2003**, *36*, 2021.
[12] B. Philip, E. Jewell, P. Greenwood, C. Weirman, *J Manuf Process* **2016**, *22*, 185.
[13] F. De Rossi, J. A. Baker, D. Beynon, K. E. A. Hooper, S. M. P. Meroni, D. Williams, Z. Wei, A. Yasin, C. Charbonneau, E. H. Jewell, T. M. Watson, *Adv. Mater. Technol.* **2018**, *3*, 1.
[14] Y. Hu, Y. Chu, Q. Wang, Z. Zhang, Y. Ming, A. Mei, Y. Rong, H. Han, *Joule* **2019**, *3*, 2076..
[15] Y. Rong, Y. Hu, A. Mei, H. Tan, M. I. Saidaminov, S. I. Seok, M. D. McGehee, E. H. Sargent, H. Han, *Science* **2018**, *361*, 6408.
[16] J. Qi, B. Zhang, Y. Ma, D. Xu, K. Chen, J. Liu, Z. Wu, Z. Xu, H. Zhou, *Adv. Mater.* **2025**, *2506114*, 1.
[17] K. S. Keremane, S. Prathapani, L. J. Haur, A. Bruno, A. Priyadarshi, A. V. Adhikari, S. G. Mhaisalkar, *ACS Appl. Energy Mater.* **2021**, *4*, 249.
[18] A. Bashir, J. H. Lew, S. Shukla, D. Gupta, T. Baikie, S. Chakraborty, R. Patidar, A. Bruno, S. Mhaisalkar, Z. Akhter, *Sol Energy* **2018**, *182*, 225.
[19] S. M. P. Meroni, K. E. A. Hooper, T. Dunlop, J. A. Baker, D. Worsley, C. Charbonneau, T. M. Watson, *Energies* **2020**, *13*, 1589.

[20] C. Worsley, P. S. jane, D. Hughes, W. C. Tsoi, T. Watson, *Mater. Adv.* **2024**, *5*, 4354.
[21] P. S. jane, B. R, T. Dunlop, K. Lacey, C. Worsley, T. Watson, J. Griffin, M. L. Davies, *Adv. Funct. Mater.* **2024**, *34*, 2401959.
[22] G. Grancini, C. Roldán-Carmona, I. Zimmermann, E. Mosconi, X. Lee, D. Martineau, S. Narbey, F. Oswald, F. De Angelis, M. Graetzel, M. K. Nazeeruddin, *Nat. Commun.* **2017**, *8*, 1.
[23] R. Cheacharoen, C. C. Boyd, G. F. Burkhard, T. Leijtens, J. A. Raiford, K. A. Bush, S. F. Bent, J. M. Luther, M. D. McGehee, *Sustain Energy Fuels [Internet]* **2018**, *2*, 2398.
[24] R. Cheacharoen, N. Rolston, D. Harwood, K. A. Bush, R. H. Dauskardt, M. D. McGehee, *Energy Environ. Sci.* **2018**, *11*, 144.
[25] K. A. Bush, A. F. Palmstrom, Z. J. Yu, M. Boccard, R. Cheacharoen, J. P. Mailoa, D. P. McMeekin, R. L. Z. Hoye, C. D. Bailie, T. Leijtens, I. M. Peters, M. C. Minichetti, N. Rolston, R. Prasanna, S. Sofia, D. Harwood, W. Ma, F. Moghadam, H. J. Snaith, T. Buonassisi, Z. C. Holman, S. F. Bent, M. D. McGehee, *Nat. Energy* **2017**, *2*, 17009.
[26] J. Chakar, F. Oswald, A. M. Dubois, E. Stéphan, S. Narbey, J. Parra, N. Molina, G. Reiss, A. Kahn, J.-Y. Lee, *Sol. RRL* **2024**, *2400093*, 1.
[27] X. Li, M. Tschumi, H. Han, S. S. Babkair, R. A. Alzubaydi, A. A. Ansari, S. S. Habib, M. K. Nazeeruddin, S. M. Zakeeruddin, M. Grätzel, *Energy Technol.* **2015**, *3*, 551.
[28] S. Pitchaiya, N. Eswaramoorthy, V. Madurai Ramakrishnan, M. Natarajan, D. Velauthapillai, *ACS Appl. Mater. Interfaces* **2022**, *14*, 43050.
[29] S. M. P. Meroni, Y. Mouhamad, F. De Rossi, A. Pockett, J. Baker, R. Escalante, J. Searle, M. J. Carnie, E. Jewell, G. Oskam, T. M. Watson, *Sci. Technol. Adv. Mater.* **2018**, *19*, 1.
[30] A. L. Palma, F. Matteocci, A. Agresti, S. Pescetelli, E. Calabro, L. Vesce, S. Christiansen, M. Schmidt, A. Di Carlo, *IEEE J. Photovoltaics* **2017**, *7*, 1674.
[31] Y. Mouhamad, S. M. P. Meroni, F. De Rossi, J. Baker, T. M. Watson, J. Searle, E. H. Jewell, *Sol Energy [Internet]* **2019**, *187*, 129.
[32] L. Shi, M. P. Bucknall, T. L. Young, M. Zhang, L. Hu, J. Bing, D. S. Lee, J. Kim, T. Wu, N. Takamure, D. R. McKenzie, S. Huang, M. A. Green, A. W. Y. Ho-Baillie, *Science* **2020**, *368*, 1328.
[33] E. J. Juarez-Perez, Z. Hawash, S. R. Raga, L. K. Ono, Y. Qi, *Energy Environ. Sci.* **2016**, *9*, 3406.
[34] Y. Xiao, C. Wang, K. K. Kondamareddy, N. Cheng, P. Liu, Y. Qiu, M. Li, Y. Liu, Y. Qi, *ACS Appl. Energy Mater.* **2018**, *1*, 5453.
[35] S. G. Hashmi, D. Martineau, X. Li, M. Ozkan, A. Tiihonen, M. I. Dar, T. Sarikka, S. M. Zakeeruddin, J. Paltakari, P. D. Lund, M. Grätzel, *Adv. Mater. Technol.* **2017**, *2*, 4.
[36] H. Lakhiani, T. Dunlop, F. De Rossi, S. Dimitrov, R. Kerremans, C. Charbonneau, T. Watson, J. Barbé, W. C. Tsoi, *Adv. Funct. Mater.* **2019**, *29*, 1900885.
[37] C. A. Worsley, T. Dunlop, S. J. Potts, R. Bolton, E. Jewell, T. M. Watson, *J. Mater. Chem.* **2024**, *12*, 9401.
[38] C. Ling, Y. Xia, X. Xiao, X. Chen, Z. Zheng, M. Xia, Y. Hu, A. Mei, Y. Rong, H. Han, *Small Methods* **2022**, *6*, 1.
[39] J. Li, J. Dagar, O. Shargaieva, O. Maus, M. Remec, Q. Emery, D. Neher, S. Albrecht, *Adv. Energy Mater.* **2025**, *15*, 2403844.
[40] R. K. Gupta, D. K. Kumar, V. Sudhakar, J. M. Beckedahl, A. Abate, E. A. Katz, L. Etgar, *Adv. Energy Mater.* **2024**, *15*, 2403844,.
[41] T. Du, W. Xu, S. Xu, S. R. Ratnasingham, C.-T. Lin, J. Kim, J. Briscoe, M. A. McLachlan, J. R. Durrant, *J. Mater. Chem. C* **2020**, *8*, 12648.
[42] Y. Cheng, Z. Zheng, S. Liu, J. Xiang, C. Han, M. Xia, G. Zhang, J. Qi, Y. Ma, K. Chen, Y. Tao, X. Lu, A. Mei, H. Han, *Adv. Energy Mater.* **2024**, *14*, 1.
[43] Y. Cheng, J. Xiang, X. Li, G. Zhang, M. Xia, C. Han, Z. Zheng, L. Chen, K. Chen, Y. Ma, J. Qi, A. Mei, H. Han, *Adv. Mater.* **2025**, *37*, 1.
[44] M. V. Khenkin, E. A. Katz, A. Abate, G. Bardizza, J. J. Berry, C. Brabec, F. Brunetti, V. Bulovic, G. Colella, C. A. J. De Wolf, A. Di Carlo, N. K. Eling, C. Forberich, R. A. J. Janssen, T. Kirchartz, J. S. Mattheis, J. Minar, I. Mora-Sero, M. Moser, S. B. L. Perini, H. J. Snaith, M. Tress, M. Saliba, *Nat. Energy* **2020**, *5*, 35.
[45] R. Tsuji, Y. Nagano, K. Oishi, E. Kobayashi, S. Ito, *Materials (Basel)* **2024**, *17*, 0.
[46] S. J. Potts, C. Phillips, T. Claypole, E. Jewell, *Coatings* **2020**, *10*, 1008.
[47] S. J. Potts, C. Phillips, E. Jewell, B. Clifford, Y. C. Lau, T. Claypole, *J Coatings Technol Res* **2020**, *17*, 447.
[48] C. A. Worsley, T. O. Dunlop, P. S. jane, R. Garcia-rodriguez, R. S. Bolton, M. L. Davies, T. Watson, *ACS Appl Energy Mater.* **2024**, *7*, 1938.